

RESEARCH

Open Access



# A pathogenic mutation in the ALS/FTD gene *VCP* induces mitochondrial hypermetabolism by modulating the permeability transition pore

Silke Vanderhaeghe<sup>1,2,3†</sup>, Jovan Prerad<sup>3†</sup>, Arun Kumar Tharkeshwar<sup>4,5</sup>, Elien Goethals<sup>1,3</sup>, Katlijn Vints<sup>6</sup>, Jimmy Beckers<sup>1,2</sup>, Wendy Scheveneels<sup>1,2</sup>, Eveline Debroux<sup>3</sup>, Katrien Princen<sup>3</sup>, Philip Van Damme<sup>1,7</sup>, Marc Fivaz<sup>3\*</sup>, Gerard Griffioen<sup>3\*</sup> and Ludo Van Den Bosch<sup>1,2\*</sup>

## Abstract

Valosin-containing protein (VCP) is a ubiquitously expressed type II AAA<sup>+</sup> ATPase protein, implicated in both amyotrophic lateral sclerosis (ALS) and frontotemporal dementia (FTD). This study aimed to explore the impact of the disease-causing *VCP*<sup>R191Q/wt</sup> mutation on mitochondrial function using a CRISPR/Cas9-engineered neuroblastoma cell line. Mitochondria in these cells are enlarged, with a depolarized mitochondrial membrane potential associated with increased respiration and electron transport chain activity. Our results indicate that mitochondrial hypermetabolism could be caused, at least partially, by increased calcium-induced opening of the permeability transition pore (mPTP), leading to mild mitochondrial uncoupling. In conclusion, our findings reveal a central role of the ALS/FTD gene *VCP* in maintaining mitochondrial homeostasis and suggest a model of pathogenesis based on progressive alterations in mPTP physiology and mitochondrial energetics.

**Keywords** Amyotrophic lateral sclerosis, Frontotemporal dementia, VCP, Mitochondria, Mitochondrial dysfunction, Mitochondrial permeability transition pore

<sup>†</sup>Silke Vanderhaeghe and Jovan Prerad: Co-first authors.

\*Correspondence:

Marc Fivaz

[marc.fivaz@remynd.com](mailto:marc.fivaz@remynd.com)

Gerard Griffioen

[gerard.griffioen@ext.remynd.com](mailto:gerard.griffioen@ext.remynd.com)

Ludo Van Den Bosch

[ludo.vandenbosch@kuleuven.be](mailto:ludo.vandenbosch@kuleuven.be)

<sup>1</sup> Laboratory of Neurobiology, Department of Neurosciences, Experimental Neurology and Leuven Brain Institute (LBI), KU Leuven – University of Leuven, Leuven, Belgium

<sup>2</sup> Laboratory of Neurobiology, VIB-KU Leuven Center for Brain & Disease Research, Leuven, Belgium

<sup>3</sup> reMYND, Leuven, Belgium

<sup>4</sup> Department of Human Genetics, KU Leuven – University of Leuven, Leuven, Belgium

<sup>5</sup> KU Leuven Institute for Single Cell Omics (LISCO), KU Leuven – University of Leuven, Leuven, Belgium

<sup>6</sup> Electron Microscopy Platform and VIB-Bioimaging Core, VIB-KU Leuven Center for Brain & Disease Research, Leuven, Belgium

<sup>7</sup> Department of Neurology, University Hospitals Leuven, Leuven, Belgium

## Introduction

Valosin-containing protein (VCP), also referred to as p97, Ter94 or Cdc48, is a highly conserved and ubiquitously expressed type II ATPase associated with diverse cellular activities (AAA<sup>+</sup>) protein [1]. Discovered by Peters *et al.* [2], VCP utilizes the chemical energy provided by ATP hydrolysis to structurally remodel target molecules [3]. As predicted by its sheer abundance, constituting up to 1% of total cellular protein, VCP is involved in a plethora of processes in a cofactor-dependent manner [4, 5]. These pathways include, but are not limited to, DNA repair, protein quality control, turnover and degradation, chromatin remodelling and organelle formation and degradation [4, 6–8].

Over 50 pathogenic *VCP* mutations have been identified to cause progressive, autosomal dominant VCP multisystem proteinopathy 1 (MSP1) [9–12], a rare disorder



progressively affecting the muscles, brain, motor neurons and bone, accompanied by TDP-43 pathology [13, 14]. Close to 10% of individuals with *VCP* mutations develop amyotrophic lateral sclerosis (ALS), with these mutations accounting for 1 to 2% of familial ALS [9, 11, 15, 16] and also being identified in sporadic ALS cases [16–18]. Furthermore, 30% of patients carrying *VCP* mutations develop frontotemporal dementia (FTD), proposed to account for 3.5% of all FTD cases [9–11, 15]. ALS and FTD are the two extremes of a neurodegenerative disease spectrum, linked through clinical, pathological (e.g. TDP-43 aggregates) and genetic overlap (e.g. mutations in *C9orf72*) [19, 20].

ALS is a fatal, adult-onset neurodegenerative disorder characterized by the selective degeneration of motor neurons in the motor cortex, brainstem and spinal cord. This motor neuron deterioration results in progressive muscle weakness and atrophy, evolves into paralysis and ultimately leads to death of the patient typically due to respiratory failure. On the other hand, FTD is characterised by a progressive loss of neurons in the frontal and anterior temporal cortices, causing personality and behavioural changes and gradual impairment of language skills [19–21]. ALS and FTD patients have an average survival after disease onset of 2–5 years and 6–14 years, respectively [22]. In line with ALS and FTD being part of the same disease spectrum, *VCP* patients with concomitant ALS and FTD have been reported [16, 19, 23–25].

Despite decades of ALS- and FTD-related drug research, both diseases remain largely untreatable and the current available therapies focus on symptom management and improving the quality of life. A notable exception is the recently discovered antisense oligonucleotide tofersen, which slows down disease progression in ALS patients carrying mutations in *SOD1* [26, 27]. The absence of effective cures is mostly due to the complexity and the incomplete understanding of the molecular mechanism causing both neurodegenerative diseases. There is substantial evidence linking mitochondrial dysfunction to both ALS and FTD [28–32], including defects in mitochondrial transport [33–36], elevated levels of oxidative stress [37–41] and structural mitochondrial defects [42–44], among others. Many of these defects occur prior to disease onset, and a (causative) mitochondrial role is further supported by the importance of mitochondria in supporting the high metabolic demand of neurons [28, 45, 46]. Interestingly, pathogenic mutations in genes associated with mitochondrial function and homeostasis, such as *CHCHD10*, *TBKI* and *VCP*, have been implicated in the development of both ALS and FTD [47, 48].

To better understand how mitochondrial dysfunction contributes to ALS/FTD-associated neurodegeneration,

we aimed to elucidate the molecular mechanisms by which the pathogenic *VCP*<sup>R191Q/wt</sup> mutation contributes to ALS/FTD-associated neurodegeneration. As most of the MSP1-associated mutations, the R191Q mutation is present in the domain linking the N-domain and the ATPase domain D1 (N-D1 linker) of the gene and has been found in both ALS and FTD patients [23]. We used CRISPR/Cas9-mediated genome editing to create a non-overexpression and screenable *VCP*<sup>R191Q/wt</sup> model in the BE(2)-M17 neuroblastoma cell line. This model allowed us to investigate the impact of the mutation on mitochondrial health and function. We discovered that the *VCP*<sup>R191Q/wt</sup> mutation results in the opening of the mitochondrial permeability transition pore (mPTP), causing mitochondrial depolarization and hypermetabolism, thereby decreasing mitochondrial health. Furthermore, our data suggest a role for mitochondrial calcium overload as the underlying cause of the mitochondrial permeability transition pore opening, thus providing a molecular mechanism by which *VCP*-related mitochondrial dysfunction may contribute to neurodegeneration in ALS and FTD.

## Materials and methods

### Cell culture

A heterozygous *VCP*<sup>R191Q/wt</sup> line and its isogenic control line (further referred to as wildtype, WT) were generated by Applied StemCell (Applied StemCell Inc., California, USA), starting from human BE(2)-M17 neuroblastoma cells (ATCC-CRL-2267, LGC Standards GmbH, Wesel, Germany). Confirmation of the *VCP*<sup>R191Q</sup> mutation was obtained following Sanger sequencing (Fig. S1A). Additionally, we confirmed that *VCP* protein levels were unaffected by the CRISPR/Cas9 treatment and insertion of the mutation (Fig. S1B and C). The isogenic line stems from a CRISPR/Cas9 treatment condition where insertion of the mutation was unsuccessful. Three isogenic WT lines were created and we confirmed that these clones showed similar results compared to the original BE(2)-M17 line during TMRM time trace experiments (Fig. S2A). Four *VCP*<sup>R191Q/wt</sup> clones were generated for each line and were found to show similar results during TMRM time trace experiments (Fig. S2B). Subsequently, one clone was selected for each line for subsequent experiments (indicated in bold, Fig. S2). Cells were grown and maintained at 37 °C and 5% CO<sub>2</sub> in Opti-MEM medium (31985-070, GIBCO, Waltham, US) enriched with 10% fetal bovine serum (FBS, 26140-079, GIBCO), 1% minimum essential medium with non-essential amino acids (MEM NEAA, 11140-035, GIBCO), 1% sodium pyruvate (11360-707, GIBCO) and 0.5% antibiotic/antimycotic solution (ABAM, 15240-062, GIBCO). Subculturing was performed using Dulbecco's phosphate buffered saline

(DPBS, 14190-094, GIBCO) and 0.05% Trypsin–EDTA (25300-054, GIBCO). Mycoplasma contamination was routinely tested using the MycoAlert Mycoplasma Detection Kit (LT07-318, Lonza, Basel, Switzerland).

#### Transmission electron microscopy (TEM)

Cells were plated 48 h prior to treatment at a concentration of 1,000,000 cells/10 cm<sup>2</sup> dish. Cells were fixed by adding double strength fixative solution (5% glutaraldehyde; 16220, EMS, Hatfield, USA) in 0.2 M sodium cacodylate buffer (12300, EMS) to the growth medium while rotating. After 10 min the solution was replaced by single strength fixative (2.5% glutaraldehyde in 0.1 M sodium cacodylate buffer) and stored overnight at 4 °C. After washes with 0.1 M sodium cacodylate buffer, the cells were scraped and pelleted. Subsequently, the pellet was cut into small cubes, which were post-fixed in 1% osmium tetroxide (19151, EMS) for 2 h, washed with dH<sub>2</sub>O and subjected to gradual dehydration through an ethanol series (50–100%). During the 70% ethanol step, the cubes were stained with uranyl acetate (22400, EMS) for 30 min at 4 °C. After dehydration, cells were infiltrated with resin (Agar 100; AGR1043, Agar Scientific, Stansted, UK)/ethanol mixtures. The following day, the cubes of cells were embedded in 100% epoxy resin at the bottom of pyramid shaped BEEM<sup>®</sup> capsules for two days at 60 °C. Next, 70 nm sections were cut on a Leica Ultracut S ultramicrotome (Leica Microsystems, Wetzlar, Germany) and collected on 200 mesh grids. Afterwards, they were post-stained with 3% uranyl acetate in water (10 min), Reynold's lead citrate (2 min). Micrographs were taken in a TEM JEOL JEM1400-LaB6 (Jeol, Tokyo, Japan) operated at 80 kV. Diameter and perimeter of mitochondria were quantified using ImageJ (WT n=371, *VCPR191Q/wt* n=377; across three independent experiments).

#### Immunocytochemistry

Cells were plated 24 h prior to fixation to reach 75% confluence. Cells were fixed using 4% paraformaldehyde (PFA, 28908, Thermo Fisher Scientific, Waltham, US) in DPBS (14190-250, Thermo Fisher Scientific) for 20 min. Three DPBS wash steps were followed by 20 min permeabilization in 0.1% Triton X-100 (T8787, Sigma-Aldrich, St. Louis, US) in DPBS. Subsequently, blocking was performed using 5% normal donkey serum (NDS, D9663, Sigma-Aldrich) in 0.1% triton X-100/DPBS for 30 min at room temperature. Primary antibodies (see Table 1) were incubated overnight in 2% NDS in Triton X-100/DPBS at 4 °C. The following day, after three DPBS wash steps, 1 µg/ml Hoechst 33342 (62249, Thermo Fisher Scientific) and the appropriate secondary antibodies (see Table 1) were incubated in 2% NDS in Triton X-100/DPBS for 1 h at RT. Finally, cells were washed three times in DPBS

and preserved in 0.1% Triton X-100/DPBS. Single plane confocal images were obtained using the Operetta CLS equipped with a 40X or 63X water emersion objective lens (Perkin Elmer, Waltham, US). Mitochondrial mass was quantified as TOMM20 intensity per cell (masked by  $\alpha$ -tubulin staining), averaged per well and normalised to WT TOMM20 intensity and was analysed with the Harmony high-content analysis software (Perkin Elmer).

#### Western Blot

Ice cold RIPA buffer (Sigma-Aldrich) supplemented with a protease inhibitor cocktail (cOmplete<sup>™</sup> EDTA-free, Sigma-Aldrich) and phosphatase inhibitors (PhosSTOP, Sigma-Aldrich) was used to lyse human neuroblastoma cells. The protein concentration was determined using the Micro BCA Protein Assay Kit (23235, Thermo Fisher Scientific) according to the protocol. Equal amounts of protein (20 µg) were supplemented with Pierce reducing sample buffer (39000, Thermo Fisher Scientific) and boiled for 10 min at 95 °C before being loaded on 4–20% Mini-PROTEAN TGX Stain-Free Precast Gels (Bio-Rad Laboratories, Hercules, US) and transferred to Trans-Blot Turbo Mini 0.2 µm nitrocellulose membranes (Bio-Rad Laboratories) using the Trans-Blot<sup>®</sup> Turbo<sup>™</sup> Transfer System (Bio-Rad Laboratories). The membranes were subsequently blocked in 5% non-fat dry milk (Blotting-Grade Blocker, Bio-Rad Laboratories) in Tris Buffered Saline solution with 0.1% tween (TBS-T, Sigma-Aldrich) for 1 h at room temperature before overnight incubation with primary antibodies (see Table 1). Three TBS-T washes and a 1 h incubation with secondary antibodies (polyclonal goat anti-rabbit/mouse-immunoglobulins/HRP, DAKP, 1/5000 in T-BST) at room temperature were performed before washing two times with TBS-T and once with TBS. Finally, protein detection was performed using enhanced chemiluminescence reagents (ECL substrate, Thermo Fisher Scientific) and the ImageQuant LAS 4000 biomolecular Imager (GE Healthcare). The ImageQuant TL software (version 7.0; GE Healthcare Life Sciences) was used to quantify band intensities. Protein levels were normalised to those of loading controls.

#### Mitochondrial membrane potential assay

Cells were plated 24 h prior to the experiment to reach 75% confluence. The mitochondrial membrane potential was measured using tetramethylrhodamine methyl ester perchlorate (TMRM, T668, Invitrogen, Eugene, US), diluted to 30 nM in 0.5% dimethyl sulfoxide (DMSO, D2650, Sigma-Aldrich) and loaded for 1.5 h in phenol red free Opti-MEM medium (11058-021, GIBCO; enriched with 10% FBS, 1% MEM NEAA, 1% sodium pyruvate and 0.5% ABAM), co-loaded with 50 nM Hoechst 33342 at 37 °C and 5% CO<sub>2</sub>. Under these conditions,

**Table 1** Overview of antibodies, plasmids, and products used

Reagent or resource	Source	Identifier
<b>Antibodies</b>		
$\alpha$ -tubulin (ICC 1:50/WB 1:500)	Cell Signaling Technology, Danvers, US	21255
GAPDH (1:5000)	Thermo Fisher Scientific, Waltham, US	AM4300
Tom20 (ICC 1:50/WB 1:500)	Santa Cruz Biotechnology, Dallas, US	Sc-17764
VCP (1:1000)	Thermo Fisher Scientific, Waltham, US	MA3-004
Alexa Fluor 488 donkey anti-rabbit (1:1000)	Invitrogen, Waltham, US	A21206
Alexa Fluor 555 donkey anti-mouse (1:1000)	Invitrogen, Waltham, US	A31570
<b>Mitochondrial respiratory activity chemicals</b>		
Hepes	Sigma-Aldrich, St. Louis, US	H3375 CAS: 7365-45-9
Sucrose	Thermo Fisher Scientific, Waltham, US	S-8600-60 CAS: 57-50-1
$\text{KH}_2\text{PO}_4$	Sigma-Aldrich, St. Louis, US	P0662 CAS: 7778-77-0
KCl	Merck, Darmstadt, Germany	104936 CAS: 7447-40-7
EGTA	Sigma-Aldrich, St. Louis, US	E4378 CAS: 67-42-5
$\text{MgCl}_2$	Sigma-Aldrich, St. Louis, US	M2670 CAS: 7791-18-6
BSA (fatty acid free)	Sigma-Aldrich, St. Louis, US	A6003 CAS: 9048-46-8
NaOH	Merck, Darmstadt, Germany	109913 CAS: 1310-73-2
<b>Compounds</b>		
$\alpha$ -Tocopherol (75 $\mu\text{M}$ ; 1 h)	Sigma-Aldrich, St. Louis, US	T3251 CAS: 10191-41-0
Bongkrekic acid (10 $\mu\text{M}$ ; 1 h)	Sigma-Aldrich, St. Louis, US	B6179 CAS 11076-19-0
Carbachol (15 $\mu\text{M}$ , 10.5 min)	Sigma-Aldrich, St. Louis, US	C4382 CAS: 51-83-2
Cyclosporin A (1 $\mu\text{M}$ and 10 $\mu\text{M}$ ; 1 h)	Sigma-Aldrich, St. Louis, US	30024 CAS: 59865-13-3
FK506 (10 nM and 25 $\mu\text{M}$ ; 1 h)	Abcam, Cambridge, UK	Ab120223 CAS: 104987-11-3
MCU4 (TMRM and mPTP assay: 1 and 3 $\mu\text{M}$ ; 1 h/ calcium measurements 2.5 or 5 $\mu\text{M}$ ; 1.5 h)	Tocris, Bristol, UK	7195 CAS: 371924-24-2
N-acetyl-L-cysteine (NAC) (1 mM; 2 h)	Sigma-Aldrich, St. Louis, US	A9165 CAS: 616-91-1
NIM811 (3 $\mu\text{M}$ ; 1 h)	MedChemExpress, New Jersey, USA	HY-P0025 CAS: 143205-42-9
Thapsigargin (2.5 $\mu\text{M}$ , 10.5 min)	Enzo Biochem, NY, USA	BML-PE180 CAS: 67526-95-8

TMRM operated in non-quenching mode [49]. Co-loading with 2.5  $\mu\text{M}$  oligomycin A (4110, Tocris, Bristol, UK) or 2.5  $\mu\text{M}$  Carbonyl cyanide 4-(trifluoromethoxy)

phenylhydrazone (FCCP, C2920, Sigma-Aldrich) served as positive or negative control, respectively. TMRM fluorescence was recorded at 37 °C and 5%  $\text{CO}_2$  using

the Operetta CLS equipped with a 40X water emersion objective lens and analysed (as TMRM intensity per cell, averaged per well and normalised to WT baseline TMRM intensity) with the Harmony high-content analysis software.

#### Mitochondrial oxygen consumption rate

In order to measure the mitochondrial oxygen consumption rate (OCR), 3,000,000 cells/ml were prepared in respiration buffer (20 mM Hepes, 110 mM sucrose, 10 mM  $\text{KH}_2\text{PO}_4$ , 120 mM KCl, 0.5 mM EGTA, 2 mM  $\text{MgCl}_2$  and 0.3% BSA in  $\text{dH}_2\text{O}$ , buffered to pH 7.2 with NaOH, see Table 1). The oxygen consumption was measured using the Clark electrode (Oxygraph+ System, Hansatech instruments Ltd, Pentney, UK). Upon loading of the cells in the chamber, 5 mM succinate (S3674, Sigma-Aldrich) and 8  $\mu\text{M}$  digitonin (D141, Sigma-Aldrich) were administered. After closure of the chamber and reaching stable measurements, baseline data were collected. Additionally, data were continuously collected during subsequent ADP (A2754, Sigma-Aldrich), oligomycin A (4110, Tocris) and FCCP (0453, Tocris) treatment (Fig. S3). Data were analysed using the OxyTrace+ software (Hansatech instruments) and normalized to initial  $\text{O}_2$  levels. The slopes were calculated to derive the OCR. Slopes from baseline, ADP-stimulated, oligomycin A-treatment and FCCP-treatment measurements represent state 2, state 3, proton leak and uncoupled respiration, respectively.

#### Metabolic rate assay

A 2X mitochondrial assay mix (MAM) was made by combining the 2X mitochondrial assay solution (MAS, 72303, Biolog, Hayward, US), 2 $\times$  Redox Dye MC (74353, Biolog) and 60  $\mu\text{g}/\text{ml}$  Saponin (SAE0073, Sigma-Aldrich). 30  $\mu\text{l}$  of the 2X MAM was added to the respective wells of the MitoPlate™ S-1 (14105, Biolog). Afterwards, the plate was incubated for 1 h at 37 °C to dissolve the substrates coated on the MitoPlate. Cells were collected in 1X MAS and plated on the MitoPlate at a concentration of 60,000 cells/well. Absorbance was measured for 24 h at 10-min intervals using the OmniLog® PM System (96164, Biolog), using its kinetic reading program ( $\text{OD}_{590\text{nm}}$ ). Data were obtained from the Biolog Data Analysis software (Biolog) and further analysed using Excel to calculate the slope of the increase in absorbance over the first two hours to represent ETC activity.

#### Calcein-AM-cobalt fluorescence quenching assay

Opening of the mitochondrial permeability transition pore was assessed by the quenching of calcein-AM fluorescence following cobalt treatment [50] using a

protocol adapted from Gautier et al. [51]. Cells were plated 48 h prior to readout to reach 75% confluence at the time of the experiment. Cells were loaded in phenol red free Opti-MEM medium (enriched with 10% FBS, 1% MEM NEAA, 1% sodium pyruvate and 0.5% ABAM) with 0.5  $\mu\text{M}$  Calcein AM (C3100MP, Thermo Fisher Scientific), 1  $\mu\text{M}$  MitoTracker Deep Red FM (M22426, Thermo Fisher Scientific) and 0.1  $\mu\text{M}$  Hoechst 33342 in 0.5% DMSO for 30 min at 37 °C and 5%  $\text{CO}_2$ . Subsequently, cells were additionally incubated with 2 mM  $\text{CoCl}_2$  (1.02539, Merck, Darmstadt, Germany) in 0.5% DMSO for 30 min. Calcein fluorescence was recorded at 37 °C and 5%  $\text{CO}_2$  using the Operetta CLS equipped with a 40X water emersion objective lens and analysed as calcein intensity per cell, averaged per well and normalised to WT baseline calcein intensity with the Harmony high-content analysis software.

#### Calcineurin activity assay

Calcineurin activity was measured using the cellular calcineurin phosphate activity assay (ab139464, Abcam, Cambridge, UK). Cells were plated 48 h prior to sample preparation in 10  $\text{cm}^2$  dishes to reach 90% confluence. Cells were collected in 15 ml Tris-Buffered Saline (TBS) and exposed to lysis buffer. Upon sedimentation at 150k x g, total protein concentration was determined using the micro BCA protein assay kit (23235, Thermo Fisher Scientific) and samples were further diluted in lysis buffer to 2.5  $\mu\text{g}/\mu\text{l}$  total protein. Further procedures followed the assay protocol and  $\text{OD}_{600\text{nm}}$  was measured using the GloMax Discover (GM3000, Promega, California, US). Calcineurin activity was quantified using Eq. 1 from the assay protocol ( $\text{PP2B} = \text{total} - \text{EGTA buffer}$ ).

#### DNA construct

The lentiviral vector pLV[Exp]-SYN1 > {YC4mito\_4xMito\_Clover3\_Ruby3} (mito\_FRET, VectorBuilder ID: VB230303-1194bmm), was designed by adding an N-terminal Cytochrome C Oxidase Subunit 8 (COX8) tag to a modified yellow cameleon sensor [52] under a neuronal synapsin promoter. This version replaces cyan and yellow fluorescent proteins with mClover3 and mRuby3 for increased brightness and reduced photodamage. Mito\_FRET is responsive to a broad range of calcium concentrations (KDs of 80 nM and 100  $\mu\text{M}$ ), with highest sensitivity at lower calcium concentrations. To probe higher mitochondrial calcium concentrations, we created the pRP[Exp]-CBh > {Mito-

4x}:{mito-linker}:{mRuby3(ns)}:{Linker}:{GCaMP6f} (Mito\_GCaMP6f, VectorBuilder ID: VB231031-1416faz) vector using a CMV promoter with the COX8 tag bound to a GCaMP6f-mRuby3 fusion protein with a KD of 375 nM.

### Mitochondrial calcium imaging

Cells were plated 24 h prior to the experiment at 10,000 cells per well in black, flat-bottom PhenoPlate 96-well plates (6055302 Revvity). Lentiviral vectors were thawed on ice, diluted in culture medium, and used to transduce cells at a multiplicity of infection (MOI) of 20. For the Mito\_GCaMP6f sensor, the cells were plated at 20,000 cells per well and transfected 24 h later using the lipofectamine<sup>®</sup> 2000 protocol (11668019, Thermo Fisher) with 80 ng DNA and 0.19  $\mu$ l Lipofectamine per well. After four days, cells were treated for 1.5 h with 2.5 or 5  $\mu$ M MCUi4 (a mitochondrial calcium uniporter blocker) or control DMSO. Imaging was performed on the Operetta CLS with a 40 $\times$  water immersion lens, capturing four fields per well in three Z-stacks (-3.0  $\mu$ m to 1.0  $\mu$ m). For mito\_FRET sensor, excitation was at 460–490 nm, and emissions were measured at 500–550 nm (mClover3) and 570–660 nm (FRET mRuby3), using 50% power and 300 ms exposure. For Mito\_GCaMP6f, excitation was at 460–490 nm (GCaMP6f) and 530–560 nm (mRuby3), with the respective emissions at 500–550 nm and 570–650 nm. Five replicate wells were used for each experiment at 37 °C and 5% CO<sub>2</sub> unless otherwise indicated in the figure legend. Five baseline measurements were taken at 1.5-min intervals, followed by treatment with 2.5  $\mu$ M thapsigargin (TG) (BML-PE180, Enzo Biochem, NY, USA) or 15  $\mu$ M carbachol (CB) (C4382, Sigma Aldrich) to assess mitochondrial calcium uptake, after which seven additional 1.5-min intervals were performed. Image analysis was conducted using Harmony 5.2 software, with Z-stack projections processed via Gaussian filtering and ROI definition using the Common Threshold. The standard cell tracking algorithm determined ROI locations and intensities were calculated for each channel, FRET ratios (mRuby3/mClover3) and the Mito\_GCaMP6f (GCaMP6f/mRuby3) ratios were calculated and the data were exported for further processing in Python 3.8.8. basal mitochondrial calcium levels were analyzed using the second basal timepoint and both ratios were normalized to the mean ratio of baseline time points to obtain  $\Delta F/F$  data.

### Compound treatment

Compounds were administered in 0.5% DMSO in either Opti-MEM medium with or without phenol red enriched with 10% FBS, 1% MEM NEAA, 1% sodium pyruvate and 0.5% ABAM. For used compounds see Table 1.

### Statistical analysis

Data are represented as mean  $\pm$  SEM, with each dot representing individual measurements across at least three individual experiments, unless indicated otherwise. Graphs and statistical analyses were made in GraphPad Prims 10.2.2. Data were tested for normal Gaussian distribution using the D'Agostino–Pearson omnibus normality test, Anderson–Darling test and/or Shapiro–Wilk normality test. Statistical tests are indicated in the respective figure legends.

## Results

### *VCP*<sup>R191Q/wt</sup> mutation is associated with enlarged mitochondria

To investigate the effect of the R191Q mutation in *VCP* on mitochondrial health, we used the CRISPR/Cas9 technology to introduce the mutation in one allele of the *VCP* gene in the human BE(2)-M17 neuroblastoma cell line (Fig. S1). We first assessed mitochondrial morphology, an important indicator of cellular homeostasis [53] affected in multiple ALS/FTD models [28], using transmission electron microscopy (TEM) both in control (WT) human cells and those carrying the heterozygous *VCP*<sup>R191Q/wt</sup> mutation (Fig. 1A and Fig. S4). A significant enlargement of both the mitochondrial diameter (Fig. 1B, increase of 26.8%) and perimeter (Fig. 1C, increase of 25.1%) was observed in *VCP*<sup>R191Q/wt</sup> mutant cells compared to WT. Mitochondrial elongation or shape, defined as the ratio of perimeter over diameter, on the other hand, remained unchanged (Fig. 1D). Additionally, our findings revealed no increase in total mitochondrial mass in the *VCP*<sup>R191Q/wt</sup> cell line compared to WT, measured as TOMM20 expression per cell using immunocytochemistry (Fig. 1E, F) and measured as TOMM20 protein levels using Western blot (Fig. 1G, H).

Taken together, these results point towards an enlargement of the mitochondria in cells carrying the *VCP*<sup>R191Q/wt</sup> mutation.

### Mitochondrial membrane potential is depolarized in *VCP*<sup>R191Q/wt</sup> mitochondria

The mitochondrial membrane potential ( $\Delta\Psi_m$ ), the voltage difference across the inner mitochondrial membrane (IMM) generated by the electron transport chain (ETC), is an important attribute of mitochondrial function [54]. In this study, we used TMRM, a cationic fluorescent dye that sequesters into active mitochondria based on the  $\Delta\Psi_m$ , to measure the mitochondrial membrane potential (Fig. 2A). Importantly, since no difference in mitochondrial mass was observed between WT and *VCP*<sup>R191Q/wt</sup> cells (Fig. 1E–H), TMRM fluorescent intensity specifically reflects the mitochondrial membrane potential rather than a change in total mitochondrial mass. Mitochondria

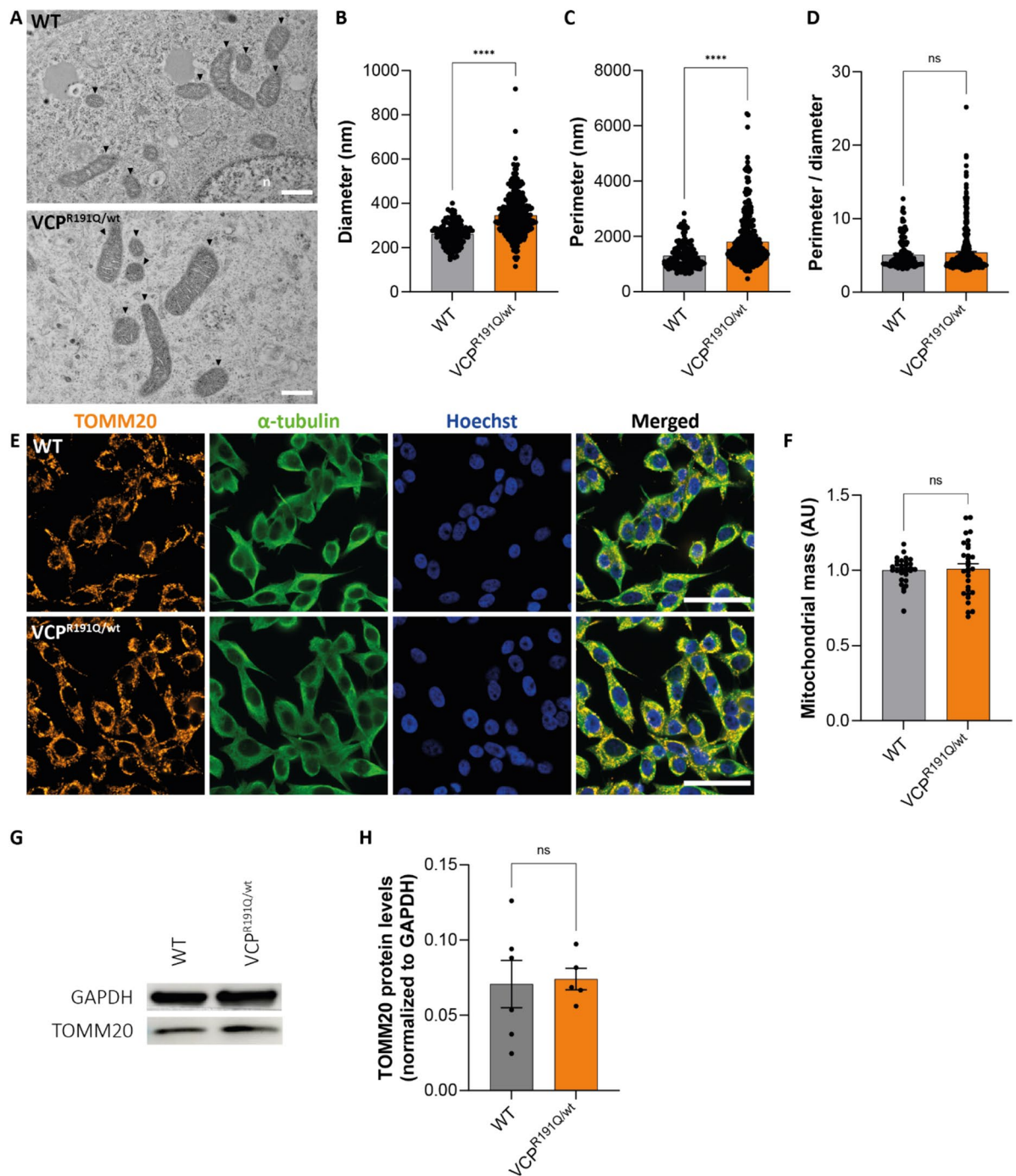


**Fig. 1** VCP<sup>R191Q/wt</sup> cells have enlarged mitochondria, but maintain mitochondrial shape and total mitochondrial mass. **A** Representative transmission electron microscopy (TEM) images of mitochondria (indicated by black arrowheads) from WT and mutant VCP<sup>R191Q/wt</sup> cell lines. Scale bar: 500 nm; (n) nucleus. **B** Diameter, **C** perimeter and **D** perimeter/diameter ratio quantifications from the TEM images shown in **A**; each dot represents a mitochondrion that was measured (WT n = 371, VCP<sup>R191Q/wt</sup> n = 377, across three independent experiments). **E** Fluorescent microscopy images of mitochondrial (TOMM20, orange) and cytoplasmic ( $\alpha$ -tubulin, green) markers in WT and VCP<sup>R191Q/wt</sup> cell lines. Single plane, scale bar: 50  $\mu$ m. **F** TOMM20 intensity quantifications, representing total mitochondrial mass, from the ICC images shown in **E**. Dots represent one well in which fluorescent intensity was measured across four independent experiments; (AU) arbitrary unit. **G** Representative Western blot detecting TOMM20 in WT and mutant VCP<sup>R191Q/wt</sup> cell lysates. GAPDH serves as loading control. **H** Quantification of Western blot shown in **G**, measuring TOMM20 levels normalised to GAPDH. Dots represent technical replicates across three independent experiments. **B–D, F** Means  $\pm$  SEM are shown. Statistical significance was evaluated by unpaired Student t-test (**B**) or Mann–Whitney test (**C, D, F, H**); ns  $p > 0.05$ , \*\*\*\* $p < 0.0001$

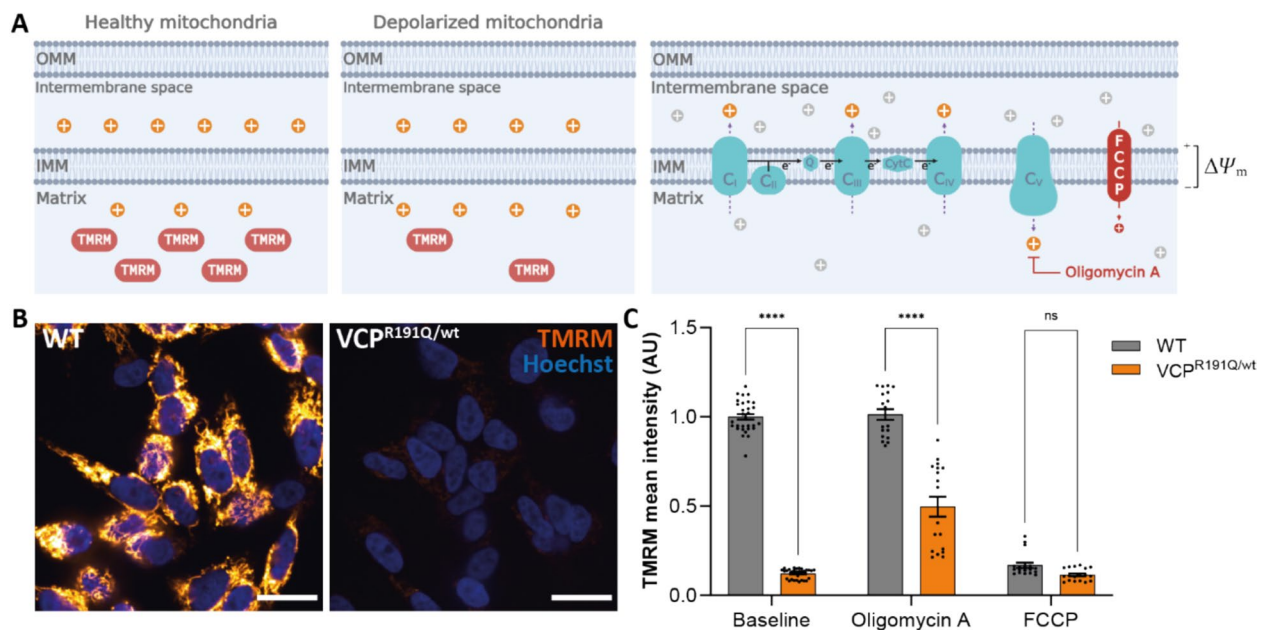


**Fig. 2** Mitochondrial membrane potential is depolarized in *VCP<sup>R191Q/wt</sup>* mitochondria. **A** The mitochondrial membrane potential ( $\Delta\Psi_m$ ) was measured by live cell imaging using TMRM, a cationic fluorescent dye, in non-quenching mode. TMRM accumulates in the mitochondrial matrix based on the mitochondrial membrane potential. In unhealthy (depolarized) mitochondria, the matrix carries comparatively fewer negative charges and consequently, less TMRM accumulates. Oligomycin A, an ATPase inhibitor causing hyperpolarization, and FCCP, a mitochondrial uncoupler causing mitochondrial depolarization, are used as positive and negative controls respectively. Abbreviations: outer mitochondrial membrane (OMM) and inner mitochondrial membrane (IMM). **B** Representative fluorescent microscopy images of mitochondria labelled with TMRM at baseline conditions. Scale bar: 20  $\mu\text{m}$ . **C** TMRM mean intensity quantifications for baseline, oligomycin A (positive control) and FCCP (negative control) conditions from the TMRM images shown in **B**. Means  $\pm$  SEM are shown; dots represent individual wells measured across four independent experiments. Statistical significance was evaluated by Two-way ANOVA with Bonferroni correction for multiple comparisons; ns  $p > 0.05$ , \*\*\*\* $p < 0.0001$

from cells carrying the *VCP<sup>R191Q/wt</sup>* mutation had a significantly reduced TMRM fluorescence indicating the depolarization of the mitochondria (Fig. 2B, C and Fig. S5). Specificity of the TMRM signal to reflect  $\Delta\Psi_m$  was confirmed by the hyperpolarization response induced by the  $F_1F_0$ -ATPase inhibitor oligomycin A and the dissipation of  $\Delta\Psi_m$  following treatment with the mitochondrial uncoupler FCCP (Fig. 2C and Fig. S2).

These findings confirm that mitochondrial health is compromised as observed by the strong depolarization across the IMM of the *VCP<sup>R191Q/wt</sup>* cells.

#### Mitochondrial oxygen consumption rate and ETC activity are increased in *VCP<sup>R191Q/wt</sup>* cells

The mitochondrial membrane potential is the result of the proton motive force maintained by the activity of the electron transport chain during cellular respiration. Therefore, one possible cause of the observed mitochondrial depolarization is a reduced activity of the electron transport chain complexes. To investigate this hypothesis, we measured ETC activity using two distinct methods.

First, we compared the oxygen consumption rate (OCR) between semi-permeabilized WT and *VCP<sup>R191Q/wt</sup>* cells using the Clark electrode, as a decrease in ETC activity should result in a corresponding decrease in oxygen consumption in mitochondria [55]. After selective permeabilization of the plasma membrane using digitonin, cells were exposed to the complex II substrate succinic acid and OCR was measured in the absence or presence of ADP. Contrary to expectation, both ADP-independent (state 2), as well as ADP-dependent (state 3) respiration were significantly increased in *VCP<sup>R191Q/wt</sup>* mitochondria (Fig. 3A). Respiration remained elevated in *VCP<sup>R191Q/wt</sup>* cells after FCCP-induced collapse of the proton gradient and concomitant mitochondrial uncoupling (Fig. 3A). Moreover, higher OCR in *VCP<sup>R191Q/wt</sup>* cells persisted after inhibition of the  $F_0F_1$ -ATPase by oligomycin A (Fig. 3A), consistent with an increased proton leak across the IMM [56],  $\Delta\Psi_m$  depolarization (Fig. 2B, C), and a compensatory ETC response to counteract a decline in proton motive force. Elevated proton permeability across the IMM is typically associated with reduced mitochondrial coupling efficiency. The respiratory coupling ratio (RCR), defined here as state 3/state 2

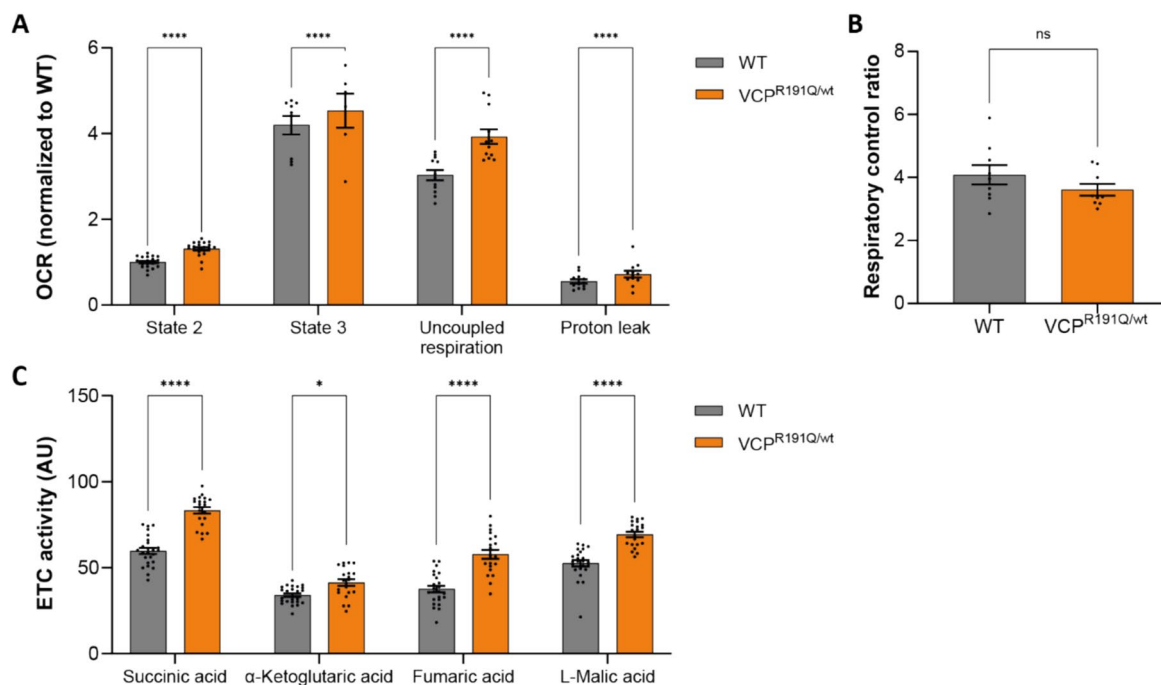


**Fig. 3** *VCP<sup>R191Q/wt</sup>* causes increased mitochondrial oxygen consumption rate and electron transport chain activity. **A** Oxygen consumption rate (OCR) in WT and *VCP<sup>R191Q/wt</sup>* cell lines: state 2 respiration following digitonin permeabilization, state 3 respiration following ADP addition, uncoupled respiration following mitochondrial uncoupling by FCCP and proton leak following oligomycin A treatment; dots represent individual measurements across at least three independent experiments. **B** Respiratory control ratio, calculated as state 3/state 2 respiration; dots represent individual measurements across at least three independent experiments. **C** Electron transport chain activity in WT and *VCP<sup>R191Q/wt</sup>* cell lines exposed to varying substrates: succinic acid, α-ketoglutaric acid, fumaric acid or L-malic acid; dots represent individual measurements across seven (*VCP<sup>R191Q/wt</sup>*) or eight (WT) independent experiments. **A–C** Means ± SEM are shown. Statistical significance was evaluated by Two-way ANOVA with Bonferroni correction for multiple comparisons (**A, C**) or unpaired Student t-test (**B**); ns  $p > 0.05$ , \* $p < 0.05$ , \*\* $p < 0.01$ , \*\*\* $p < 0.001$ , \*\*\*\* $p < 0.0001$

respiration, was not significantly different in *VCP<sup>R191Q/wt</sup>* cells, but showed a small trend towards a mild uncoupling of mitochondria (Fig. 3B). Together, these findings indicate that mitochondria in *VCP<sup>R191Q/wt</sup>* cells have a hyperactive ETC which may result from a proton leak in the mitochondrial matrix.

Second, to confirm the potential increase in electron transport chain activity, we assessed mitochondrial ETC activity using the tetrazolium redox (MC) dye [57]. Cytochrome C is the terminal electron acceptor in the ETC and its reduction is measured by a colour shift of the MC dye. Following exposure of semi-permeabilized cells to an array of mitochondrial substrates (succinic acid, α-ketoglutaric acid, fumaric acid and L-malic acid), we observed an increase in ETC electron flow in *VCP<sup>R191Q/wt</sup>* compared to WT cells (Figs. 3C and S6), confirming ETC hyperactivity in response to a broad range of TCA substrates.

In conclusion, these findings provide compelling evidence supporting increased ETC activity in mutant *VCP* cells and suggest that both dissipation of  $\Delta\Psi_m$  and mitochondrial hypermetabolism result, at least partly, from a proton leak across the mitochondrial inner membrane.

### Calcium-induced mPTP opening underlies mitochondrial depolarization

The mitochondrial permeability transition pore (mPTP) [51] is a non-selective channel that allows passage of molecules up to 1.5 kDa in size across the IMM [58–60]. Opening of the mPTP can trigger apoptosis and has been implicated in ALS as a mechanism of motoneuron death [61, 62]. We therefore evaluated the opening of the mPTP as a potential mechanism underlying the proton leak and dissipation of  $\Delta\Psi_m$  in *VCP<sup>R191Q/wt</sup>* cells. We measured opening of the mPTP by live-cell imaging using the calcein-AM- $\text{CoCl}_2$  fluorescence quenching assay. Cells were first loaded with calcein-AM and subsequently treated with  $\text{CoCl}_2$  which quenches calcein fluorescence everywhere except in the mitochondrial matrix as the IMM is impermeable to cobalt [51, 63] (Fig. 4A, B). After confirming equal calcein loading in both cell lines (Fig. 4C), we observed a decreased intensity of calcein fluorescence in mitochondria from mutant *VCP<sup>R191Q/wt</sup>* cells compared to their WT counterparts, suggesting increased opening of the mPTP in *VCP<sup>R191Q/wt</sup>* cells (Fig. 4B, D). Furthermore, rescue of calcein fluorescent intensity in

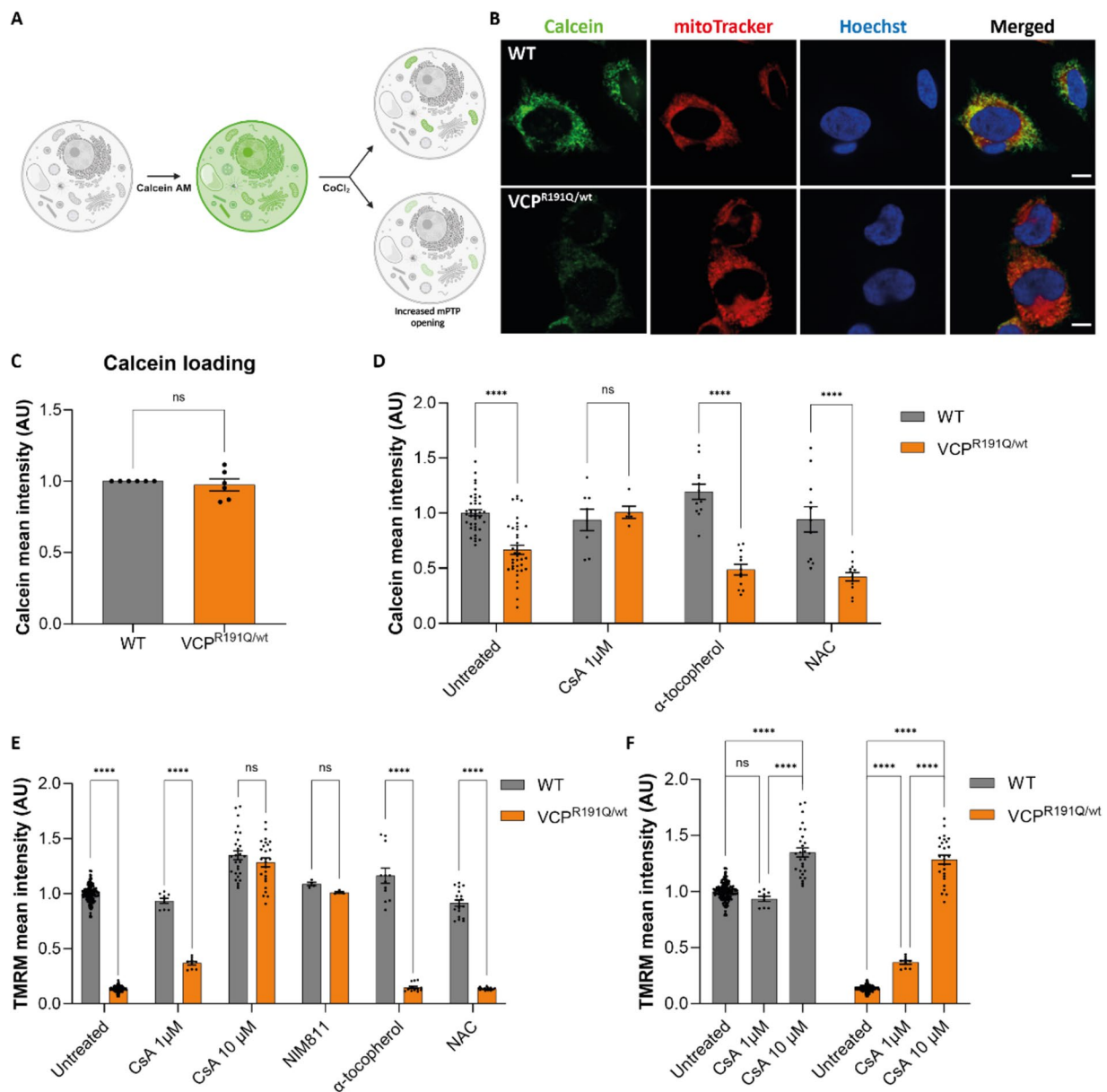


**Fig. 4** Mitochondrial PTP opening underlies mitochondrial depolarization. **A** Illustration of calcein-AMcobalt quenching assay, used to measure mitochondrial permeability transition pore (mPTP) opening during live cell imaging. Cells are loaded with calcein-AM and subsequently treated with  $\text{CoCl}_2$  which quenches calcein fluorescence everywhere except in mitochondria as the IMM is impermeable to cobalt. Decreased calcein intensity in mitochondria indicates opening of the mPTP. **B** Representative fluorescent microscopy images of WT and  $\text{VCP}^{\text{R191Q/wt}}$  cells stained with calcein (green) and mitoTracker (red). Scale bar: 10  $\mu\text{m}$ . **C** Calcein mean intensity for WT and  $\text{VCP}^{\text{R191Q/wt}}$  cells not exposed to cobalt treatment to confirm equal calcein loading. Means  $\pm$  SEM are shown; dots represent calcein mean intensity from 6 independent experiments. **D** Calcein mean intensity for WT and  $\text{VCP}^{\text{R191Q/wt}}$  cells both untreated and following exposure to mPTP inhibitor cyclosporin A (CsA) and oxidative stress induced mPTP opening-inhibitors  $\alpha$ -tocopherol and N-acetyl cysteine (NAC). **E** TMRM mean intensity for WT and  $\text{VCP}^{\text{R191Q/wt}}$  cells both untreated and following exposure to mPTP inhibitors cyclosporin A (CsA) and NIM811 and oxidative stress induced mPTP opening-inhibitors  $\alpha$ -tocopherol and N-acetyl cysteine (NAC). **F** TMRM mean intensity for WT and  $\text{VCP}^{\text{R191Q/wt}}$  cells both untreated and following exposure to mPTP inhibitor cyclosporin A (CsA). **D–F** Means  $\pm$  SEM are shown; dots represent individual measurements across at least three independent experiments. **C–F** Statistical significance was evaluated by Mann–Whitney test (**C**) or Two-way ANOVA with Bonferroni correction for multiple comparisons (**D–F**); ns  $p > 0.05$ , \* $p < 0.05$ , \*\* $p < 0.01$ , \*\*\*\* $p < 0.0001$

*VCP*<sup>R191Q/wt</sup> mitochondria following treatment with the mPTP inhibitor cyclosporin A (CsA), confirmed a role of the mPTP opening in mitochondrial release of the dye (Fig. 4D). Notably, the TMRM mean intensity in *VCP*<sup>R191Q/wt</sup> cells was significantly increased following treatment with 1  $\mu$ M CsA and fully rescued after treatment with 10  $\mu$ M CsA, further implicating mPTP opening in mitochondrial depolarization (Fig. 4E, F). CsA, besides inhibiting the mPTP, also inhibits calcineurin. To disambiguate these two CsA targets, we treated cells with FK506, a calcineurin inhibitor with no known effect on the mPTP [64], as well as NIM811, a cyclophilin D (CypD)-specific non-immunosuppressive derivative of CsA [65, 66]. Neither mPTP opening nor mitochondrial depolarization were affected by treatment with FK506 (Fig. S7A–C) at a concentration reported to quantitatively inhibit calcineurin activity (10 nM) [67]. Additionally, calcineurin activity was shown not to be affected in the *VCP*<sup>R191Q/wt</sup> cell line (Fig. S7D). In contrast, NIM811 fully restored TMRM mean intensity in *VCP*<sup>R191Q/wt</sup> cells (Fig. 4E), similar as observed following CsA treatment. To further hone in on a CypD-dependent mechanism of mPTP opening, we made use of bongkreikic acid (BKA), a drug that targets a mechanism of mPTP opening that is independent of CypD [68]. BKA treatment did not restore the mitochondrial membrane potential in *VCP*<sup>R191Q/wt</sup> cells, in line with CypD-mediated activation of mPTP in the disease state (Fig. S8). Together, these data indicate that depolarization of  $\Delta\Psi_m$  and possibly the other mitochondrial phenotypes observed in *VCP*<sup>R191Q/wt</sup> cells originate from a CypD-dependent increase in mPTP opening.

The main initiators of mitochondrial permeability transition are reactive oxygen species and mitochondrial matrix calcium overload [58–60]. To identify the trigger of mPTP opening, we first exposed cells to N-acetylcysteine (NAC), a glutathione-precursor that prevents oxidative stress-induced mPTP opening [51, 69] or  $\alpha$ -tocopherol, which inhibits mPTP opening by lipid peroxidation [51, 70]. Neither of these antioxidants reduced mPTP opening or rescued  $\Delta\Psi_m$  in *VCP*<sup>R191Q/wt</sup> cells, arguing against a role of reactive oxygen species in these processes (Fig. 4D, E).

We next investigated whether calcium overload in the mitochondrial matrix underlies mPTP opening and  $\Delta\Psi_m$  depolarization in *VCP*<sup>R191Q/wt</sup> mitochondria. Calcium influx in the matrix is primarily mediated by the mitochondrial calcium uniporter (MCU) complex [71]. Treatment with the MCU inhibitor MCUi4 (Fig. S9) attenuated mPTP opening (1  $\mu$ M; Fig. 5A) and increased  $\Delta\Psi_m$  (3  $\mu$ M; Fig. 5B) pointing to elevated mitochondrial calcium as a proximal cause of mPTP opening.

$\Delta\Psi_m$  rescue by MCUi4 is only partial, suggesting that other mechanisms contribute to  $\Delta\Psi_m$  depolarization in *VCP*<sup>R191Q/wt</sup> cells. Consistent with a role of calcium in mPTP opening, increased basal mitochondrial  $\text{Ca}^{2+}$  levels ( $[\text{Ca}^{2+}]_m$ ) were observed in the *VCP*<sup>R191Q/wt</sup> mitochondria using a mitochondria-targeted calcium FRET sensor (mito\_FRET; Fig. 5C). In addition to steady-state elevation of  $[\text{Ca}^{2+}]_m$ , mitochondrial calcium uptake was also exacerbated in these mutant cells, following thapsigargin-induced ER calcium release (Fig. 5D).

In conclusion, our findings suggest that the clinical R191Q *VCP* mutation results in mitochondrial calcium dyshomeostasis, which sets off a series of mitochondrial perturbations involving increased opening of the mPTP,  $\Delta\Psi_m$  depolarization and ETC hyperactivity. These results provide compelling evidence for mitochondrial hypermetabolism in a *VCP* knock-in cell model, a mitochondrial phenotype reminiscent of the hypermetabolism observed in individuals with ALS, both in the brain [72] and at the organismal level [73, 74].

## Discussion

Mitochondria are crucial organelles for cell homeostasis and for supporting the high metabolic requirements of neurons [75]. Throughout decades of research, mitochondrial dysfunction has been hypothesised to contribute to the neuronal degeneration associated with the ALS/FTD disease spectrum, as well as to other neurodegenerative disorders [76]. Interestingly, the type II AAA<sup>+</sup> *VCP* protein plays an important role in mitochondrial homeostasis and is involved in the regulation of mitochondrial fusion, mitochondrial calcium uptake and mitochondrial quality control, both through its involvement in mitophagy as well as in mitochondria-associated degradation [4]. Accordingly, knock-in mice with the *VCP* mutation (R155H/+), found in both ALS and FTD patients [23], show extensive accumulation of abnormal mitochondria [77, 78].

In this study, we used a non-overexpression *VCP*<sup>R191Q/wt</sup> model, generated in the neuroblastoma BE(2)-M17 cell line, to gain a deeper understanding of the molecular mechanism by which *VCP* mutations contribute to ALS/FTD-associated neurodegeneration, focusing on mitochondrial dysfunction. We found that mitochondria in our mutant *VCP*<sup>R191Q/wt</sup> cell model are enlarged and that the total mitochondrial mass is unaffected. These data imply fewer mitochondria per cell in *VCP*<sup>R191Q/wt</sup> cells and a potential defect in the mitochondrial fusion or fission machinery. Furthermore, enlarged mitochondria, with no apparent signs of matrix/cristae defects may reflect an increase in mitochondrial output [79], and would be consistent with the mitochondrial hypermetabolism we report here.

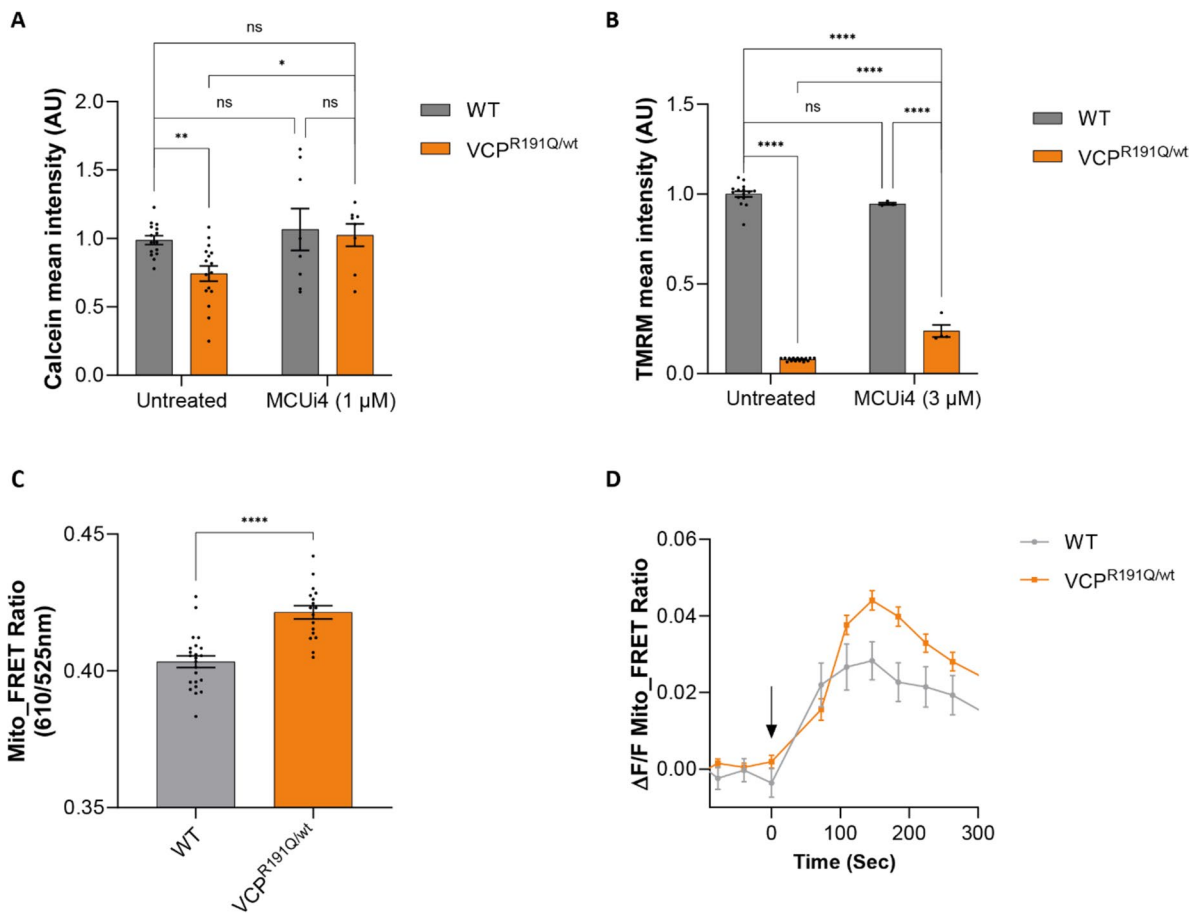


**Fig. 5** Mitochondrial PTP opening is induced by mitochondrial calcium overload in  $VCP^{R191Q/wt}$  cells. **A** Calcein mean intensity for WT and  $VCP^{R191Q/wt}$  cells both untreated and following exposure to mitochondrial calcium uptake inhibitor MCUi4. **B** TMRM mean intensity for WT and  $VCP^{R191Q/wt}$  cells both untreated and following exposure to mitochondrial calcium uptake inhibitor MCUi4. **A, B** Means  $\pm$  SEM are shown; dots represent individual wells measured across at least three independent experiments. **C** Basal Mito\_FRET ratio in WT and  $VCP^{R191Q/wt}$  cells. Mean  $\pm$  SEM are shown; dots represent individual wells measured across at least three independent experiments. **(D)** Representative normalized Mito\_FRET response to 2.5  $\mu$ M thapsigargin (arrow indicates thapsigargin addition) in WT and  $VCP^{R191Q/wt}$  cells. Mean  $\pm$  SEM of the whole cell population for each cell type are shown. Statistical significance was evaluated by Two-way ANOVA with Bonferroni correction for multiple comparisons (**A, B**) or Student's t-test (**C**); ns  $p > 0.05$ , \* $p < 0.05$ , \*\*\*\* $p < 0.0001$

Additionally, we found the mitochondrial membrane potential in  $VCP^{R191Q/wt}$  cells to be severely depolarized, a well-recognized feature in multiple ALS/FTD models that has previously been reported in different  $VCP$  disease models [80–84]. Dissipation of  $\Delta\Psi_m$  is associated with elevated oxygen consumption in all respiratory states analysed and with an increase in ETC activity, revealing a state of mitochondrial hypermetabolism in mutant  $VCP$  cells. We attribute the ETC overdrive to a compensatory response of mitochondria to restore the proton motive force, an essential feature of mitochondrial health and output. A link between  $VCP$  and mitochondrial respiration has been observed before, in a study reporting increased oxygen consumption in  $VCP$ -deficient cells [85]. Hypermetabolism (defined at the

organismal level by increased energy expenditure relative to energy intake) is often observed in ALS patients and is an important prognostic factor [86, 87], but the cellular origin of this metabolic state is unclear. Our findings suggest that ETC overdrive may contribute to this global energy imbalance, at least in ALS/FTD linked to  $VCP$ .

Several independent lines of evidence point to increased proton permeability across the IMM as one probable cause for depolarization of  $\Delta\Psi_m$  in  $VCP^{R191Q/wt}$  cells. First, oxygen consumption remains higher in mutant cells after inhibition of the  $F_1F_0$ -ATPase, a phenotype that often reflects an adaptive response from the ETC to counteract a proton leak. Second, although not statistically significant, we observed a trend towards mild mitochondrial uncoupling in  $VCP^{R191Q/wt}$  cells, a

typical consequence of a proton leak. Third, we demonstrated increased opening of the mPTP in mutant cells, which is a known cause for mitochondrial depolarization and uncoupling [58, 88]. Finally, and most importantly, blockade of the mPTP by CypD-targeting drugs restored  $\Delta\Psi_m$  in the *VCP* cell line, indicating that mitochondrial depolarization is a direct consequence of mPTP opening. Notably, calcium accumulation in the mitochondrial matrix, which we identify as one possible trigger for mPTP opening, can also cause depolarization of  $\Delta\Psi_m$  (independently of the mPTP), by virtue of the positive charge of this bivalent cation [89]. An impact of *VCP* on mitochondrial proton permeability is also consistent with an independent study showing that pathogenic *VCP* mutations induce mitochondrial uncoupling [85]. mPTP opening is unlikely to be the sole mechanism underlying  $\Delta\Psi_m$  depolarization in *VCP* mutant cells, because CyD-targeting drugs and the MCU blocker MCUi4 only partially rescue  $\Delta\Psi_m$  at concentrations that fully inhibit mPTP opening (Fig. 4D–F and 5A, B). Another likely cause of  $\Delta\Psi_m$  dissipation is increased activity of the  $F_1F_o$ -ATPase at steady state (state 3 respiration), which is reflected by larger TMRM responses to oligomycin A in *VCP*<sup>R191Q/wt</sup> cells (Fig. 2C and Fig. S2).

We show evidence for mitochondrial calcium dyshomeostasis in *VCP*<sup>R191Q/wt</sup> cells, in the form of elevated basal  $[Ca^{2+}]_m$  and increased calcium uptake following ER calcium release. Calcium-induced mPTP opening may therefore be a compensatory mechanism to release excessive calcium from this organelle [90, 91], although the involvement of the mPTP in calcium efflux remains controversial [92]. How steady-state  $[Ca^{2+}]_m$  remains elevated in *VCP*<sup>R191Q/wt</sup> cells in the face of increased mPTP opening is unclear. One possibility is that the rate of calcium influx exceeds that of calcium efflux through the mPTP, a scenario in line with high mitochondrial calcium uptake in *VCP*<sup>R191Q/wt</sup> cells (Fig. 5D). Alternatively, mitochondrial calcium efflux through the transition pore could be negligible under the relatively mild conditions of mPTP activation in these cells [92].

The evidence described in this study, linking a clinical *VCP* mutation to the mPTP, is of immediate relevance for ALS/FTD, given the central role of this pore in cell death and as a prominent drug target. A current multiconductance model for mPTP opening proposes two functionally distinct pores: a high-conductance pore whose prolonged opening is implicated in mitochondrial swelling and apoptosis, and a low-conductance pore involved in the regulation of physiological processes, including mitochondrial calcium homeostasis [93]. Other than CypD, the molecular constituents of the mPTP and the structural differences between high and low conductivity

pores are poorly characterized and highly debated. Based on the lack of obvious signs of mitochondrial swelling and cell death/toxicity in *VCP*<sup>R191Q/wt</sup> cells, we favour activation of a low conductance pore in *VCP*<sup>R191Q/wt</sup> cells, although we cannot exclude transient, low frequency opening of a high conductance pore.

How expression of the pathogenic *VCP*<sup>R191Q</sup> mutation leads to calcium-induced activation of the mPTP is an open question that will be the object of future studies. One possibility is that *VCP* protects against mPTP opening by facilitating the degradation of ubiquitinated MICU1 [94, 95], an essential accessory subunit of the MCU [96] and the target of the inhibitor MCUi4. Alternatively, *VCP* could control calcium transport from the ER to mitochondria at the mitochondria-ER contacts sites (MERCS) which have been previously implicated in ALS pathogenesis [34, 84, 97]. *VCP* is known to impact endoplasmic reticulum-mitochondria contact through interaction with VPS13D [97] and together with VAPB, it is among the most relevant MERC controllers in ALS/FTD pathogenesis [98].

In conclusion, our findings reveal a central role of the ALS/FTD gene *VCP* in modulation of the mPTP and mitochondrial bioenergetics. Based on these results, we propose a two-tier model of ALS pathogenesis with, initially, an adaptive mitochondrial metabolic response to subtle increases in mPTP opening. With time, ETC overdrive results in accelerated mitochondrial aging, with increased production of reactive oxygen species at respiratory complexes, reduced calcium buffering and compromised ATP production. Around disease onset, mitochondria have fully transitioned from a hypermetabolic state to a dysfunctional state, culminating in full-blown activation of the mPTP and mitochondrial death pathways in motor neurons. This mito-centric disease model identifies mitochondrial calcium homeostasis and mPTP modulators as potential drug targets.

## Supplementary Information

The online version contains supplementary material available at <https://doi.org/10.1186/s40478-024-01866-0>.

Supplementary Material 1

Supplementary Material 2

## Acknowledgements

We thank all members of the Laboratory of Neurobiology for valuable discussions and insightful suggestions. We thank Pieter Vermeersch for input on the OCR experiments and Geert Bultynck for the insights into calcium-induced mPTP opening. We thank the VIB Bioimaging and TEM Core for the use of the equipment and for practical help during the experiments. Graphics were created using BioRender.com

## Author contributions

SV designed and performed the majority of the experiments, analysed the data and drafted the manuscript. JP designed and performed some of the

OCR experiments and designed and performed ETC activity experiments. AKT and KV performed the TEM experiments and provided input on the data. EG and JV performed the calcium FRET experiments. JB and WS performed Western blot experiments. ED, KP, PVD, MF, GG and LVDB supervised the experiments and discussed the results. All authors helped with editing of the manuscript. All authors read the final version of the manuscript and agreed with its content.

### Funding

SV is funded by VLAIO Baekeland mandate HBC.2019.2575. This work was supported by VIB, KU Leuven (C1 and “Opening the Future” Fund), the “Fund for Scientific Research Flanders” (FWO-Vlaanderen), the Thierry Latran Foundation, the “Association Belge contre les Maladies neuro-Musculaires—aide à la recherche ASBL” (ABMM), the Muscular Dystrophy Association (MDA), the ALS Liga België (A Cure for ALS), Target ALS, and the ALS Association (ALSA). reMYND is supported by Flanders Innovation & Entrepreneurship (VLAIO), formerly known as the Institute for the Promotion of Innovation by Science and Technology, in Flanders (Grants 030383, 070157, 080394, and 090494 to G.G.). PVD holds a clinical investigatorship of the FWO and is supported by the E. von Behring Chair for Neuromuscular and Neurodegenerative Disorders, the Fund ‘Een Hart voor ALS’, and the ‘Laevers Fund for ALS Research’. LVDB is supported by the Genetec Award for Rare Diseases.

### Availability of data and materials

Data available upon request. The VCP<sup>R191Q</sup> BE(2)-M17 cell line is available from GG under a material transfer agreement with reMYND.

### Declarations

#### Ethics approval and consent to participate

Not applicable.

#### Competing interests

PVD has served in advisory boards for Biogen, CSL Behring (King of Prussia, US), Alexion Pharmaceuticals (Boston, US), Ferrer (Barcelona, Spain), QurAlis (Cambridge, UK), Cytokinetics (South San Francisco, US), Argenx (Boston, US), UCB (Brussels, Belgium), Muna Therapeutics, Alector (South San Francisco, US), Augustine Therapeutics (Leuven, Belgium), VectorY (Amsterdam, Netherlands), Zambon (Bresso, Italy), Amylyx (Cambridge, UK) (paid to institution). P.V.D. has received speaker fees from Biogen and Amylyx (paid to institution). PVD is supported by the E. von Behring Chair for Neuromuscular and Neurodegenerative Disorders (from CSL Behring, paid to institution). ED, KP and MF own reMYND warrants. GG is a consultant for reMYND and owns reMYND warrants and shares. LVDB is head of the Scientific Advisory Board of Droia Ventures (Meise, Belgium). LVDB is a scientific founder of Augustine Therapeutics.

Received: 14 August 2024 Accepted: 23 September 2024

Published online: 10 October 2024

### References

- Xia D, Tang WK, Ye Y (2016) Structure and function of the AAA+ ATPase p97/Cdc48p. *Gene* 583:64–77
- Peters JM, Walsh MJ, Franke WW (1990) An abundant and ubiquitous homo-oligomeric ring-shaped ATPase particle related to the putative vesicle fusion proteins Sec18p and NSF. *EMBO J* 9:1757–1767
- Snider J, Thibault G, Houry WA (2008) The AAA+ superfamily of functionally diverse proteins. *Genome Biol* 9:1–8
- Chu S, Xie X, Payan C, Stochaj U (2023) Valosin containing protein (VCP): initiator, modifier, and potential drug target for neurodegenerative diseases. *Mol Neurodegener* 18:52
- Buchberger A, Schindelin H, Hänzelmann P (2015) Control of p97 function by cofactor binding. *FEBS Lett* 589:2578–2589
- Braxton JR, Southworth DR (2023) Structural insights of the p97/VCP AAA+ ATPase: how adapter interactions coordinate diverse cellular functionality. *J Biol Chem* 299:105182
- Jentsch S, Rumpf S (2007) Cdc48 (p97): a “molecular gearbox” in the ubiquitin pathway? *Trends Biochem Sci* 32:6–11
- van den Boom J, Meyer H (2018) VCP/p97-mediated unfolding as a principle in protein homeostasis and signaling. *Mol Cell* 69:182–194
- Korb M, Peck A, Alfano LN, Berger KI, James MK, Ghoshal N et al (2022) Development of a standard of care for patients with valosin-containing protein associated multisystem proteinopathy. *Orphanet J Rare Dis* 17:1–15
- Saracino D, Clot F, Camuzat A, Anquetil V, Hannequin D, Guyant-Maréchal L et al (2018) Novel VCP mutations expand the mutational spectrum of frontotemporal dementia. *Neurobiol Aging* 72:187.e11–187.e14
- Al-Obeidi E, Al-Tahan S, Surampalli A, Goyal N, Wang AK, Hermann A et al (2018) Genotype–phenotype study in patients with valosin-containing protein mutations associated with multisystem proteinopathy. *Clin Genet* 93:119–125
- Johnson MA, Klickstein JA, Khanna R, Gou Y, Raman M (2022) The Cure VCP Scientific Conference 2021: molecular and clinical insights into neurodegeneration and myopathy linked to multisystem proteinopathy-1 (MSP-1). *Neurobiol Dis* 169:1–11
- Kim HJ, Kim NC, Wang YD, Scarborough EA, Moore J, Diaz Z et al (2013) Mutations in prion-like domains in hnRNPA2B1 and hnRNPA1 cause multisystem proteinopathy and ALS. *Nature* 495:467–473
- Kimonis VE, Kovach MJ, Waggoner B, Leal S, Salam A, Rimer L et al (2000) Clinical and molecular studies in a unique family with autosomal dominant limb-girdle muscular dystrophy and Paget disease of bone. *Genet Med* 2:232–241
- Mehta SG, Khare M, Ramani R, Watts GDJ, Simon M, Osann KE et al (2013) Genotype-phenotype studies of VCP-associated inclusion body myopathy with Paget disease of bone and/or frontotemporal dementia. *Clin Genet* 83:422–431
- Koppers M, van Blitterswijk MM, Vlam L, Rowicka PA, van Vught PWJ, Groen EJM et al (2012) VCP mutations in familial and sporadic amyotrophic lateral sclerosis. *Neurobiol Aging* 33:837.e7–837.e13
- Abramzon Y, Johnson JO, Scholz SW, Taylor JP, Brunetti M, Calvo A et al (2012) Valosin-containing protein (VCP) mutations in sporadic amyotrophic lateral sclerosis. *Neurobiol Aging* 33:2231.e1–2231.e6
- Ayaki T, Ito H, Fukushima H, Inoue T, Kondo T, Ikemoto A et al (2014) Immunoreactivity of valosin-containing protein in sporadic amyotrophic lateral sclerosis and in a case of its novel mutant. *Acta Neuropathol Commun* 2:1–14
- Scarian E, Fiamingo G, Diamanti L, Palmieri I, Gagliardi S, Pansarasa O (2022) The role of VCP mutations in the spectrum of amyotrophic lateral sclerosis—frontotemporal dementia. *Front Neurol* 13:1–15
- Ling SC, Polymenidou M, Cleveland DW (2013) Converging mechanisms in ALS and FTD: disrupted RNA and protein homeostasis. *Neuron* 79:416–438
- Kirola L, Mukherjee A, Mutsuddi M (2022) Recent updates on the genetics of amyotrophic lateral sclerosis and frontotemporal dementia. *Mol Neurobiol* 59:5673–5694
- Kansal K, Mareddy M, Sloane KL, Minc AA, Rabins PV, McGready JB et al (2016) Survival in frontotemporal dementia phenotypes: a meta-analysis. *Dement Geriatr Cogn Disord* 41:109–122
- Johnson JO, Mandrioli J, Benatar M, Abramzon Y, Van Deerlin VM, Trojanowski JQ et al (2010) Exome sequencing reveals VCP mutations as a cause of familial ALS. *Neuron* 68:857–864
- Feng S-Y, Lin H, Che C-H, Huang H-P, Liu C-Y, Zou Z-Y (2022) Phenotype of VCP mutations in Chinese amyotrophic lateral sclerosis patients. *Front Neurol* 13:1–11
- Miura S, Hiruki S, Okada T, Takei SI, Senzaki K, Okada Y et al (2023) Case report: frontotemporal dementia and amyotrophic lateral sclerosis caused by a missense variant (p.Arg89Trp) in the valosin-containing protein gene. *Front Genet* 14:1–8
- Miller T, Cudkovicz M, Shaw PJ, Andersen PM, Atassi N, Bucelli RC et al (2020) Phase 1–2 trial of antisense oligonucleotide tofersen for SOD1 ALS. *N Engl J Med* 383:109–119
- Miller TM, Cudkovicz ME, Genge A, Shaw PJ, Sobue G, Bucelli RC et al (2022) Trial of antisense oligonucleotide tofersen for SOD1 ALS. *N Engl J Med* 387:1099–1110
- Smith EF, Shaw PJ, De Vos KJ (2019) The role of mitochondria in amyotrophic lateral sclerosis. *Neurosci Lett* 710:1–17

29. Magrané J, Cortez C, Gan W-B, Manfredi G (2014) Abnormal mitochondrial transport and morphology are common pathological denominators in SOD1 and TDP43 ALS mouse models. *Hum Mol Genet* 23:1413–1424
30. Khalil B, Liévens JC (2017) Mitochondrial quality control in amyotrophic lateral sclerosis: towards a common pathway? *Neural Regen Res* 12:1052–1061
31. Kodavati M, Wang H, Hegde ML (2020) Altered mitochondrial dynamics in motor neuron disease: an emerging perspective. *Cells* 9:1–23
32. Lines G, Casey JM, Preza E, Wray S (2020) Modelling frontotemporal dementia using patient-derived induced pluripotent stem cells. *Mol Cell Neurosci* 109:1–23
33. Iovino M, Agathou S, González-Rueda A, Del Castillo V-H, Borroni B, Alberici A et al (2015) Early maturation and distinct tau pathology in induced pluripotent stem cell-derived neurons from patients with MAPT mutations. *Brain* 138:3345–3359
34. Guo W, Naujock M, Fumagalli L, Vandoorne T, Baatsen P, Boon R et al (2017) HDAC6 inhibition reverses axonal transport defects in motor neurons derived from FUS-ALS patients. *Nat Commun* 8:1–14
35. Fazal R, Boeynaems S, Swijsen A, De Decker M, Fumagalli L, Moisse M et al (2021) HDAC6 inhibition restores TDP-43 pathology and axonal transport defects in human motor neurons with TARDBP mutations. *EMBO J* 40:1–24
36. Fumagalli L, Young FL, Boeynaems S, De Decker M, Mehta AR, Swijsen A et al (2021) C9orf72-derived arginine-containing dipeptide repeats associate with axonal transport machinery and impede microtubule-based motility. *Sci Adv* 7:1–20
37. Onesto E, Colombrita C, Gumina V, Borghi MO, Dusi S, Doretti A et al (2016) Gene-specific mitochondrial dysfunctions in human TARDBP and C9ORF72 fibroblasts. *Acta Neuropathol Commun* 4:1–14
38. Said Ahmed M, Hung WY, Zu JS, Hockberger P, Siddique T (2000) Increased reactive oxygen species in familial amyotrophic lateral sclerosis with mutations in SOD1. *J Neurol Sci* 176:88–94
39. Barber SC, Shaw PJ (2010) Oxidative stress in ALS: key role in motor neuron injury and therapeutic target. *Free Radic Biol Med* 48:629–641
40. Mitsumoto H, Santella R, Liu X, Bogdanov M, Zipprich J, Wu HC et al (2008) Oxidative stress biomarkers in sporadic ALS. *Amyotroph Lateral Scler* 9:177–183
41. Ehrlich M, Hallmann AL, Reinhardt P, Araúzo-Bravo MJ, Korr S, Röpke A et al (2015) Distinct neurodegenerative changes in an induced pluripotent stem cell model of frontotemporal dementia linked to mutant TAU protein. *Stem Cell Rep* 5:83–96
42. Atsumi T (1981) The ultrastructure of intramuscular nerves in amyotrophic lateral sclerosis. *Acta Neuropathol* 55:193–198
43. Higgins CMJ, Jung C, Xu Z (2003) ALS-associated mutant SOD1G93A causes mitochondrial vacuolation by expansion of the intermembrane space by involvement of SOD1 aggregation and peroxisomes. *BMC Neurosci* 4:1–14
44. Sasaki S, Iwata M (2007) Mitochondrial alterations in the spinal cord of patients with sporadic amyotrophic lateral sclerosis. *J Neuropathol Exp Neurol* 66:10–16
45. Misgeld T, Schwarz TL (2017) Mitostasis in neurons: maintaining mitochondria in an extended cellular architecture. *Neuron* 96:651–666
46. Schwarz TL (2013) Mitochondrial trafficking in neurons. *Cold Spring Harb Perspect Med* 5:1–16
47. Anderson CJ, Bredvik K, Burstein SR, Davis C, Meadows SM, Dash J et al (2019) ALS/FTD mutant CHCHD10 mice reveal a tissue-specific toxic gain-of-function and mitochondrial stress response. *Acta Neuropathol* 138:103–121
48. Harding O, Evans CS, Ye J, Cheung J, Maniatis T, Holzbaur ELF (2021) ALS-And FTD-associated missense mutations in TBK1 differentially disrupt mitophagy. *Proc Natl Acad Sci USA* 118:1–11
49. Perry SW, Norman JP, Barbieri J, Brown EB, Gelbard HA (2011) Mitochondrial membrane potential probes and the proton gradient: a practical usage guide. *Biotechniques* 50:98–115
50. Petronilli V, Miotto G, Canton M, Brini M, Colonna R, Bernardi P et al (1999) Transient and long-lasting openings of the mitochondrial permeability transition pore can be monitored directly in intact cells by changes in mitochondrial calcein fluorescence. *Biophys J* 76:725–734
51. Gautier CA, Giaime E, Caballero E, Ndez L, Song Z, Chan D et al (2012) Regulation of mitochondrial permeability transition pore by PINK1. *Mol Neurodegener* 7:1–15
52. Miyawaki A, Griesbeck O, Heim R, Tsien RY (1999) Dynamic and quantitative  $Ca^{2+}$  measurements using improved cameleons. *Proc Natl Acad Sci* 96:2135–2140
53. Campello S, Scorrano L (2010) Mitochondrial shape changes: orchestrating cell pathophysiology. *EMBO Rep* 11:678–684
54. Zorova LD, Popkov VA, Plotnikov EY, Silachev DN, Pevzner IB, Jankauskas SS et al (2018) Mitochondrial membrane potential. *Anal Biochem* 552:50–59
55. Gnaiger E et al (2020) Mitochondrial physiology. *Bioenerg Commun* 2020(1):1–44
56. Affourtit C, Quinlan CL, Brand MD (2012) Measurement of proton leak and electron leak in isolated mitochondria. In: Palmeira CM, Moreno AJ (eds) *Mitochondrial bioenergetics: methods and protocol*. Humana Press, Totowa, pp 165–182
57. Lei X-H, Bochner BR (2021) Optimization of cell permeabilization in electron flow based mitochondrial function assays. *Free Radic Biol Med* 177:48–57
58. Bernardi P, Gerle C, Halestrap AP, Jonas EA, Karch J, Mnatsakanyan N et al (2023) Identity, structure, and function of the mitochondrial permeability transition pore: controversies, consensus, recent advances, and future directions. *Cell Death Differ* 30:1869–1885
59. Endlicher R, Drahota Z, Štefková K, Červinková Z, Kučera O (2023) The Mitochondrial permeability transition pore—current knowledge of its structure, function, and regulation, and optimized methods for evaluating its functional state. *Cells* 12:1–17
60. Halestrap AP (2009) What is the mitochondrial permeability transition pore? *J Mol Cell Cardiol* 46:821–831
61. Liu X, Xu S, Wang P, Wang W (2015) Transient mitochondrial permeability transition mediates excitotoxicity in glutamate-sensitive NSC34D motor neuron-like cells. *Exp Neurol* 271:122–130
62. Yu CH, Davidson S, Harapas CR, Hilton JB, Mlodzianoski MJ, Laohamonthonkul P et al (2020) TDP-43 triggers mitochondrial DNA release via mPTP to activate cGAS/STING in ALS. *Cell* 183:636–649
63. Petronilli V, Miotto G, Canton M, Colonna R, Bernardi P, Di Lisa F (1998) Imaging the mitochondrial permeability transition pore in intact cells. *BioFactors* 8:263–272
64. Connern CP, Halestrap AP (1994) Recruitment of mitochondrial cyclophilin to the mitochondrial inner membrane under conditions of oxidative stress that enhance the opening of a calcium-sensitive non-specific channel. *Biochem J* 302(Pt 2):321–4
65. Zulian A, Rizzo E, Schiavone M, Palma E, Tagliavini F, Blaauw B et al (2014) NIM811, a cyclophilin inhibitor without immunosuppressive activity, is beneficial in collagen VI congenital muscular dystrophy models. *Hum Mol Genet* 23:5353–5363
66. Waldmeier PC, Zimmermann K, Qian T, Tintelnot-Blomley M, Lemasters JJ (2003) Cyclophilin D as a drug target. *Curr Med Chem* 10:1485–1506
67. Bierer BE, Mattila PS, Standaert RF, Herzenberg LA, Burakoff SJ, Crabtree G et al (1990) Two distinct signal transmission pathways in T lymphocytes are inhibited by complexes formed between an immunophilin and either FK506 or rapamycin. *Proc Natl Acad Sci* 87:9231–9235
68. Baines CP (2009) The molecular composition of the mitochondrial permeability transition pore. *J Mol Cell Cardiol* 46:850–857
69. Reid AB, Kurten RC, McCullough SS, Bronck RW, Hinson JA (2007) Mechanisms of chloroform-induced hepatotoxicity: oxidative stress and mitochondrial permeability transition in freshly isolated mouse hepatocytes. *J Pharmacol Exp Ther* 312:509–516
70. Yorimitsu M, Muranaka S, Sato EF, Hirofumi F, Kouichi A, Tatsuji Y et al (2004) Role of alpha-tocopherol in the regulation of mitochondrial permeability transition. *Physiol Chem Phys Med NMR* 36:95–107
71. Marchi S, Pinton P (2014) The mitochondrial calcium uniporter complex: molecular components, structure and physiopathological implications. *J Physiol* 592:829–839
72. Cistaro A, Valentini MC, Chiò A, Nobili F, Calvo A, Moglia C et al (2012) Brain hypermetabolism in amyotrophic lateral sclerosis: a FDG PET study in ALS of spinal and bulbar onset. *Eur J Nucl Med Mol Imaging* 39:251–259
73. Bouteloup C, Desport JC, Clavelou P, Guy N, Derumeaux-Burel H, Ferrier A et al (2009) Hypermetabolism in ALS patients: an early and persistent phenomenon. *J Neurol* 256:1236–1242

74. Fayemendy P, Marin B, Labrunie A, Boirie Y, Walrand S, Achamrah N et al (2021) Hypermetabolism is a reality in amyotrophic lateral sclerosis compared to healthy subjects. *J Neurol Sci* 420:1–5
75. Murali Mahadevan H, Hashemiaghdam A, Ashrafi G, Harbauer AB (2021) Mitochondria in neuronal health: from energy metabolism to Parkinson's disease. *Adv Biol* 5:1–18
76. Wilson DM, Cookson MR, Van Den Bosch L, Zetterberg H, Holtzman DM, Dewachter I (2023) Hallmarks of neurodegenerative diseases. *Cell* 186:693–714
77. Yin HZ, Nalbandian A, Hsu CI, Li S, Llewellyn KJ, Mozaffar T et al (2012) Slow development of ALS-like spinal cord pathology in mutant valosin-containing protein gene knock-in mice. *Cell Death Dis* 3:1–12
78. Nalbandian A, Llewellyn KJ, Badadani M, Yin HZ, Nguyen C, Katheria V et al (2013) A progressive translational mouse model of human valosin-containing protein disease: the VCP<sup>R155H/+</sup> mouse. *Muscle Nerve* 47:260–270
79. Masuda T, Wada Y, Kawamura S (2016) ES1 is a mitochondrial enlarging factor contributing to form mega-mitochondria in zebrafish cones. *Sci Rep* 6:22360
80. Kim NC, Tresse E, Kolaitis RM, Mollieux A, Thomas RE, Alami NH et al (2013) VCP is essential for mitochondrial quality control by PINK1/Parkin and this function is impaired by VCP mutations. *Neuron* 78:65–80
81. Braun RJ, Zischka H, Madeo F, Eisenberg T, Wissing S, Bu S et al (2006) Crucial mitochondrial impairment upon CDC48 mutation in apoptotic yeast. *J Biol Chem* 281:25757–25767
82. Chang YC, Hung WT, Chang YC, Chang HC, Wu CL, Chiang AS et al (2011) Pathogenic VCP/TER94 alleles are dominant actives and contribute to neurodegeneration by altering cellular ATP level in a drosophila IBMPFD model. *PLoS Genet* 7:1–18
83. Ludtmann MHR, Arber C, Bartolome F, De Vicente M, Preza E, Carro E et al (2017) Mutations in valosin-containing protein (VCP) decrease ADP/ATP translocation across the mitochondrial membrane and impair energy metabolism in human neurons. *J Biol Chem* 292:8907–8917
84. Hall CE, Yao Z, Choi M, Tyzack GE, Serio A, Luisier R et al (2017) Progressive motor neuron pathology and the role of astrocytes in a human stem cell model of VCP-related ALS. *Cell Rep* 19:1739–1749
85. Bartolome F, Wu HC, Burchell VS, Preza E, Wray S, Mahoney CJ et al (2013) Pathogenic VCP mutations induce mitochondrial uncoupling and reduced ATP levels. *Neuron* 78:57–64
86. Ferri A, Coccorello R (2017) What is “hyper” in the ALS Hypermetabolism? *Mediat Inflamm* 2017:1–11
87. Steyn FJ, Ioannides ZA, Van Eijk RPA, Heggie S, Thorpe KA, Ceslis A et al (2018) Hypermetabolism in ALS is associated with greater functional decline and shorter survival. *J Neurol Neurosurg Psychiatry* 89:1016–1023
88. Reichert SA, Kim-Han JS, Dugan LL (2001) The mitochondrial permeability transition pore and nitric oxide synthase mediate early mitochondrial depolarization in astrocytes during oxygen-glucose deprivation. *J Neurosci* 21:6608–6616
89. Duchen MR (2000) Mitochondria and calcium: from cell signalling to cell death. *J Physiol* 529(Pt 1):57–68
90. Agarwal A, Wu PH, Hughes EG, Fukaya M, Tischfield MA, Langseth AJ et al (2017) Transient opening of the mitochondrial permeability transition pore induces microdomain calcium transients in astrocyte processes. *Neuron* 93:587–605
91. Lu X, Kwong JQ, Molkenin JD, Bers DM (2016) Individual cardiac mitochondria undergo rare transient permeability transition pore openings. *Circ Res* 118:834–841
92. De Marchi E, Bonora M, Giorgi C, Pinton P (2014) The mitochondrial permeability transition pore is a dispensable element for mitochondrial calcium efflux. *Cell Calcium* 56:1–13
93. Bonora M, Giorgi C, Pinton P (2022) Molecular mechanisms and consequences of mitochondrial permeability transition. *Nat Rev Mol Cell Biol* 23:266–285
94. Stoll S, Xi J, Ma B, Leimena C, Behringer EJ, Qin G et al (2019) The valosin-containing protein protects the heart against pathological Ca<sup>2+</sup> overload by modulating Ca<sup>2+</sup> uptake proteins. *Toxicol Sci* 171:473–484
95. Lizano P, Rashed E, Stoll S, Zhou N, Wen H, Hays TT et al (2017) The valosin-containing protein is a novel mediator of mitochondrial respiration and cell survival in the heart in vivo. *Sci Rep* 7:1–11
96. Mallilankaraman K, Doonan P, Cárdenas C, Chandramoorthy HC, Müller M, Miller R et al (2012) MICU1 is an essential gatekeeper for mcu-mediated mitochondrial Ca<sup>2+</sup> uptake that regulates cell survival. *Cell* 151:630–644
97. Du Y, Wang J, Xiong J, Fang N, Ji WK (2021) VPS13D interacts with VCP/p97 and negatively regulates endoplasmic reticulum–mitochondria interactions. *Mol Biol Cell* 32:1474–1486
98. Chen J, Bassot A, Giuliani F, Simmen T (2021) Amyotrophic lateral sclerosis (ALS): stressed by dysfunctional mitochondria-endoplasmic reticulum contacts (MERCs). *Cells* 10:1–20

## Publisher's Note

Springer Nature remains neutral with regard to jurisdictional claims in published maps and institutional affiliations.